Reprinted from
ICARUS 87, 140–155 (1990)

Impact Spallation Experiments: Fracture Patterns and Spall Velocities[1]

CAROL A. POLANSKEY[2] AND THOMAS J. AHRENS[3]

Lindhurst Laboratory of Experimental Geophysics, Division of Geological and Planetary Sciences, California Institute of Technology, Pasadena, California 91125

Received December 8, 1986; revised February 1, 1990

Spall velocities were measured for nine experimental impacts into San Marcos gabbro targets. Impact velocities ranged from 1 to 6.5 km/sec. Projectiles were iron, aluminum, lead, and basalt of varying sizes. The projectile masses ranged from a 4-g lead bullet to a 0.04-g aluminum sphere. The velocities of fragments were measured from high-speed films taken of the events. The maximum spall velocity observed was 30 m/sec, or 0.56 percent of the 5.4 km/sec impact velocity. The measured velocities were compared to the spall velocities predicted by the spallation model of Melosh (1984). The compatibility between the spallation model for large planetary impacts and the results of these small-scale experiments is considered in detail. The targets were also bisected to observe the pattern of internal fractures. The series of fractures was observed, whose location coincided with the boundary between rock subjected to the peak shock compression and a theoretical "near-surface zone" predicted by the spallation model. According to the model, between this boundary and the free surface, the target material is expected to have received reduced levels of compressive stress as compared to the more highly shocked region below.

INTRODUCTION

In this paper we present results of experiments designed to constrain theories of spallation in high-velocity impacts. Spallation, the separation of large fragments from a free surface as a result of dynamic tensile failure, is of interest because it is a mechanism that may eject lightly shocked material from planetary and asteroidal surfaces.

Much of the recent interest in spallation has resulted from the discovery that the meteorite ALHA81005 appears to be of lunar origin (Marvin 1984), and the SNC meteorites (shergottites, nakhlites, and Chassigny) may have originated on Mars (McSween and Stolper 1980, Wood and Ashwal 1981). McSween (1985) gives an extensive review of the SNC meteorite literature pertaining to their composition and unique characteristics. The absence of shock metamorphism of the nakhlites has motivated a search for mechanisms capable of accelerating impact ejecta to a Martian escape velocity of 5 km/sec without subjecting it to high, peak-shock pressures. These criteria pose a problem because the Hugoniot equation of state for one-dimensional planar flow determines a direct relation between particle and free surface velocities and the shock pressure. This relation implies that achieving particle velocities near 2.5 km/sec (and free-surface velocities of 5 km/sec) by direct shock requires shock pressures of 20 to 30 GPa. Several models have been proposed to accelerate impact ejecta to the Martian es-

[1] Contribution number 4405 from the Division of Geological and Planetary Sciences, California Institute of Technology, Pasadena, California 91125.

[2] Present address: Jet Propulsion Laboratory, California Institute of Technology, 4800 Oak Grove Drive, Pasadena, CA 91109.

[3] To whom correspondence should be addressed.

0019-1035/90 $3.00

cape velocity. One of these is the Melosh (1984) impact spallation model. We will address the predictions of this model for ejection velocity, fragment size, and peak shock-pressure distributions at length below.

In the past, spallation has been studied at near-surface and surface explosion craters in alluvium (Stump and Reinke 1984). Evidence of impact spallation could be inferred from numerical models (Ahrens and O'Keefe 1978), showing the production of lightly shocked ejecta originating near the free surface. Moreover, Vickery (1986) finds evidence for relatively high-velocity ejecta from analyses of lunar and Martian secondary craters. Whether these ejecta are launched by the spall mechanism is not clear. Vickery (1986, 1987) does conclude that fragments with characteristic dimensions on the order of tens of meters could not be launched to speeds such that these escape from either the Moon or Mars by the spall mechanism. However, there are no published values of spall velocities measured from experimental impacts.

Aside from constraining the origin of the SNC meteorites, another context in which spallation is of interest is in the evolution of asteroids (and by implication, planetesimals in the early solar system). Here we are concerned with impacts that occur under such low gravity that strength effects are important on a large scale. As crater size decreases, the fraction of material ejected by spallation increases. On the largest asteroids (surface gravity 0.1 m/sec^2), not only is gravity less important for craters with depths as great as 50 m (Gaffney 1978), but the likely low strength of the regolith on these bodies may lead to the escape of a substantial fraction of the ejecta by spallation (Cintala *et al.* 1979). This process may be important in the evolution of asteroid families and belts (Capaccioni *et al.* 1986).

The next section will describe the spallation experiments. A qualitative description of the targets will be presented along with the results of the spall velocity measurements. A preliminary discussion of the measured spall velocities was given by Polanskey and Ahrens (1985). Next, the Melosh (1984) spallation model will be reviewed with respect to its application to the present experiments. This section will include a discussion of the relationship between the proposed lightly shocked region of the target and the internal fractures observed beneath several of the experimental impact craters in this study. Vertical spall velocities predicted by the hydrodynamic ejection version of the spallation model will then be compared to the measured experimental spall velocities.

EXPERIMENTAL PROCEDURES

The spall velocity experiments were conducted in two phases. In February 1984, preliminary spall velocity measurements were made at the Caltech shock wave laboratory for two low-velocity impacts. The remaining experiments spanned a range of impact velocities and were conducted in September 1984 at the NASA Ames Vertical Gun Range (AVGR).

In all cases, the target material was San Marcos gabbro. This material has a density, ρ_t, of 2.9 g/cm^3, dynamic tensile strength, σ_t, of 0.15 GPa, and longitudinal wave velocity, c_L, of 6.4 km/sec (Lange *et al.* 1984b). To the level of approximation used in this paper, c_L is considered to be independent of stress. The compressive strength is between 3 and 6 GPa. Birch (1966) calculates the Poisson ratio, μ, for San Marcos gabbro as 0.32. A detailed characterization of the mineralogy of this rock can be found in Lange *et al.* (1984b).

For the low-velocity experiments, a 30/06 rifle was used to obtain impact velocities near 1 km/sec. The projectiles were a 4.1-g lead bullet measuring 7.8 mm in diameter and 2.4 cm in length, and a 7.9-mm-diameter aluminum sphere with a mass of 0.65 g. The aluminum projectile had been chosen to reduce the density difference between the projectile and the gabbro target. The gabbro was cut into cubes roughly 16 cm on

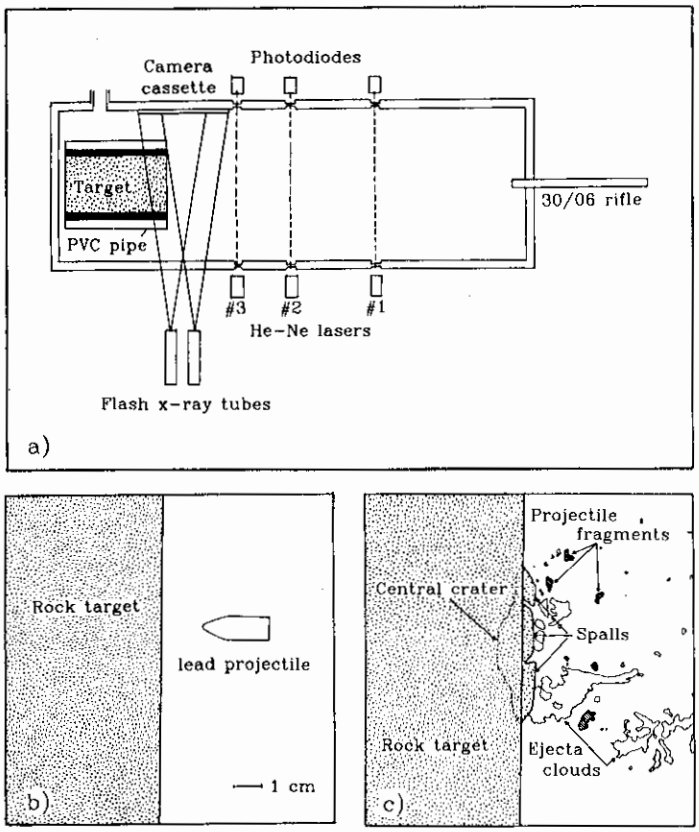

FIG. 1. (a) Sketch of experimental configuration for spall velocity measurements. The projectile velocity is determined by a counter, measuring time intervals as the projectile breaks the laser beams. The lasers also activate other counters which then trigger the x-ray tubes. (b) Drawing of the first x-ray exposure showing the projectile in flight at approximately 20 μsec before impact. (c) Drawing of the second x-ray exposure taken approximately 300 msec later. Spall velocities are measured directly from this exposure. In addition to the spall fragments, high-speed ejecta and projectile fragments are also visible.

a side and mounted with concrete into sections of 27-cm diameter PVC pipe. The total target mass was just under 30 kg. The targets were mounted in a tank kept at atmospheric pressure. The tank contained three He–Ne lasers to measure projectile velocity (Fig. 1a). Two x-ray tubes were positioned approximately 1 m outside the tank (1.5 m from the point of impact). The first x-ray tube was timed to photograph the target immediately before impact, and the second x-ray photograph was taken of the ejecta and spall fragments 300 msec later. Spall velocities were determined by measuring the distance traveled by the spall fragments from the target surface during that time interval (Figs. 1b, 1c).

Both the low-velocity powder gun and the light gas gun were used at the AVGR, thus providing a range in impact velocities from 1.7 to 6.5 km/sec. The projectiles for these experiments were primarily 3.2-mm-diameter spheres of iron and aluminium with the addition of two slightly larger projectiles of steel and basalt. Projectile masses were between 1.06 and 0.04 g and are listed along with other experimental parameters in Table I. The targets were 23 to 30 kg unmounted blocks of San Marcos gabbro placed in a tank evacuated to 5 mm

TABLE I

EXPERIMENTAL PARAMETERS

Shot No.:	603	608	840901	840902	840904	840905	840906	840907	840909
Projectile									
Material	Pb	Al	Al	Fe	Fe	Fe	Fe	basalt	steel
a (cm)	0.391	0.397	0.159	0.159	0.159	0.159	0.159	0.238	0.318
m_p (g)	4.10	0.65	0.0443	0.1292	0.1297	0.1297	0.1297	0.1557	1.0571
ρ_p (g/cm^3)	11.3	2.56	2.64	7.74	7.74	7.74	7.74	2.75	7.90
U (km/sec)	0.89	1.01	6.49	4.60	5.44	4.60	4.76	2.26	1.69
KE (10^{10} ergs)	1.62	0.33	0.93	1.37	1.92	1.37	1.47	0.40	1.51
Target									
M_t (kg)	23	23	24	25	29	23	13	23	24
KE/M_t (10^5 erg/g)	7.0	1.4	3.9	5.5	6.6	6.0	11	1.7	6.3
Crater dimensions									
Depth (cm)	0.95	0.35	1.0	1.50	1.65	1.45	1.40	0.70	1.40
Diameter (cm)	6.3	2.2	6.5	9.8	10.5	8.0	9.2	3.5	8.3
Volume (cm^3)	9.5	0.5	9.0	30	36	19	23	2.3	25.5
Displaced mass									
M_c (g)	27.0	1.4	25.8	86	103	54.5	65.9	6.6	73.1
M_{spall} (g)	—	—	10.1	40.6	47.4	36.4	30.8	—	28.8
M_{spall}/M_c	—	—	0.39	0.47	0.46	0.67	0.47	—	0.39

Hg. The interior of the vacuum tank measured 2.5 m in diameter and 1.8 m in height. The cratering events were recorded by a Dynafax Model 350 35-mm framing camera with variable framing rates from 9000 to 35,000 frames/sec. Illumination was provided by a Cordin Model 359 strobe. The photographic equipment was located outside the vacuum tank approximately 1.5 m from the target. Figure 2 shows a series of three frames taken at 2-msec intervals from one of these films. The consecutive positions of one prominent spall fragment are marked on each frame.

After each shot, the ejecta fragments were inspected for evidence of spallation. Because spallation is a near-surface phenomenon, a spall fragment was defined to be any ejecta fragment containing part of the original surface of the target. In most cases, the top surface of the target had been polished and was easily identified. Most of the ejecta fitting the above criteria were recovered, and their locations within the tank were recorded. However, no attempt was made to search the tank in a systematic fashion, so it is unlikely that this data set is complete. The mass of each identified spall fragment, m_{spall}, was determined, and both the maximum length, l_{max}, and the thickness from the top surface to its maximum depth, t_{max}, were measured. These parameters are listed in Table II. The total mass of spall fragments collected from each impact, M_{spall}, is listed in Table I. The ratio of t_{max} to l_{max} is plotted in Fig. 3 as a function of spall mass. The average value of t_{max}/l_{max} for all the collected ejecta was 0.2, and is also very close to the average value for the fragment set from each individual experiment.

Crater volumes were determined by measuring the volume of dry No. 120 Ottawa

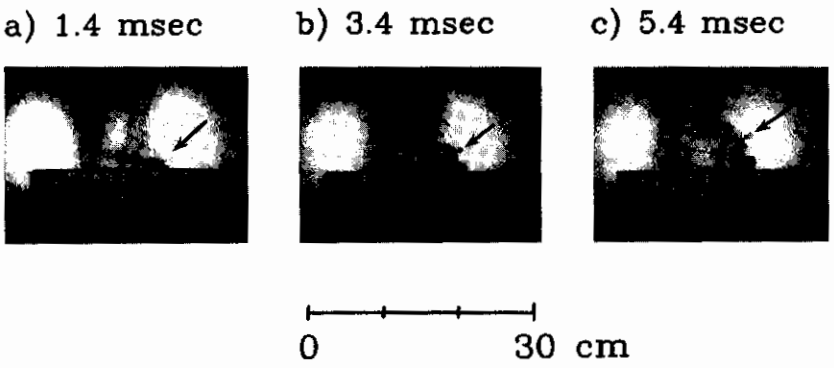

FIG. 2. Three frames from the film of shot 840904 are shown to illustrate the film coverage of the Ames experiments. The time elapsed since impact is given above each frame, and the time interval between frames is 2 msec. The spall fragment indicated by the arrows is traveling at an average vertical velocity of 8.9 m/sec. The target outline has been enhanced.

TABLE II

SPALL FRAGMENT DIMENSIONS

m_{spall} (g)	l_{max} (cm)	t_{max} (mm)	m_{spall} (g)	l_{max} (cm)	t_{max} (mm)	m_{spall} (g)	l_{max} (cm)	t_{max} (mm)
	840901			840902			840904	
4.40	5.25	4.47	10.50	5.50	8.89	15.30	5.06	9.19
0.80	1.80	4.32	8.00	4.30	8.13	9.20	4.55	7.21
0.70	1.65	3.43	7.80	4.60	8.38	5.00	4.10	6.78
0.65	1.95	3.66	6.30	3.80	6.22	4.10	3.00	7.62
0.40	1.40	3.20	2.00	2.75	5.36	2.60	2.90	6.40
0.40	1.95	2.24	1.60	2.10	5.31	2.00	2.65	6.12
0.20	1.15	2.64	1.00	2.15	6.40	1.40	2.30	5.28
0.10	0.90	1.88	0.60	1.65	4.44	0.90	2.20	4.06
0.05	0.50	0.66	0.20	1.20	1.98	0.70	2.40	2.54
0.50	0.85	1.27	0.05	0.60	0.68	0.60	2.45	4.27
						0.40	1.40	3.25
						0.30	1.25	3.00
						0.30	1.55	2.34
						0.25	1.15	3.00
	840905			840906			840906	
3.00	2.70	6.65	17.60	6.70	9.40	9.50	4.00	8.71
3.00	2.60	5.16	4.70	3.65	7.47	5.50	3.45	6.88
2.40	3.40	7.92	2.55	3.20	5.64	3.00	2.60	5.79
1.90	2.05	5.74	2.30	2.65	5.69	2.30	2.95	5.82
1.70	2.15	3.99	1.40	2.55	5.41	1.30	2.25	4.32
1.15	2.65	2.89	1.00	1.60	4.70	1.10	1.40	5.54
0.80	1.90	5.28	0.30	1.20	3.91	1.05		3.99
0.70	1.50	4.88	0.05	2.20	0.89	0.90	1.60	4.93
0.55	1.90	2.97				0.90	1.55	4.37
0.50	1.65	3.94				0.40	1.40	3.50
0.50	1.70	2.84				0.30	1.40	3.76
0.45	1.65	2.49				0.25	1.60	5.64
0.35	1.55	2.97				0.25	1.60	2.44
0.15	1.20	4.01				0.15	1.55	1.62
0.15	0.90	3.71				0.10	2.25	1.57
0.10		1.98				0.10	1.15	1.24

sand required to fill each crater. This crater volume was used to calculate the total mass of material ejected from each crater, M_e. This result ws then compared to the total mass of spall fragments collected, M_{spall}, and listed in Table 1. For these experiments, between 39 and 67% of the excavation was due to spallation. Next, the displaced mass, M_e, was scaled by the ratio of

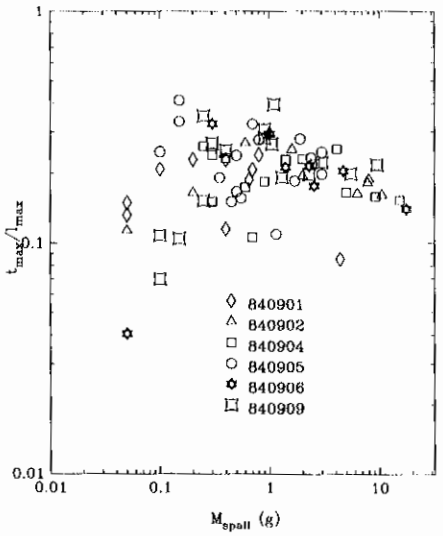

FIG. 3. The ratio of maximum vertical spall thickness, t_{max}, to maximum spall length, l_{max}, is plotted as a function of mass for each of the collected spall fragments.

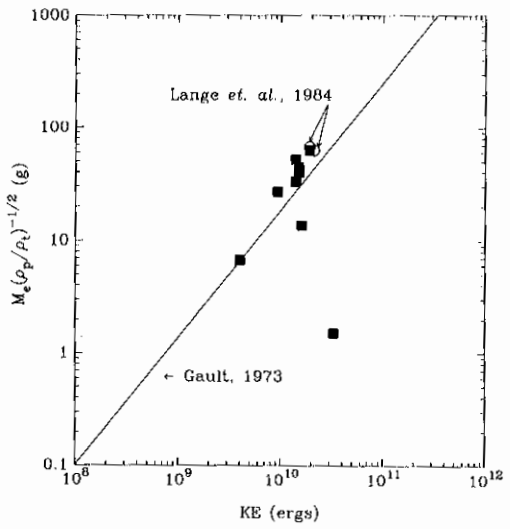

FIG. 4. Relationship between a corrected form of the displaced mass and the kinetic energy of the impact. The current results, solid squares, are plotted along with data from Lange *et al.* (1984), open circles, and a linear fit to the Gault (1973) data.

projectile to target density, and plotted as a function of projectile energy in Fig. 4. These results plot close to the curve Gault (1973) fit to data from 64 earlier impact experiments. Finally, several targets were bisected through the center of the crater in order to observe the internal fractures. The results of the fracture analysis will be presented in the next section.

RESULTS

In all cases, the craters displayed two distinct zones. The floor at the central pit of the crater was highly fractured and covered with finely crushed rock, whereas the wide, shallow, outer zone had a relatively fresh surface. It is proposed that this outer zone is the result of spallation, while the inner zone was excavated by downward and then outward and upward flow. In several cases the plan view of the outer crater perimeter was very irregular. There is also evidence of incomplete spalls in the outer zone, which were either partially separated from the target or visible only as surface cracks. On the basis of the ratio of projectile energy to target mass (given in Table I), these experiments fall into the classification of crater formation, where $KE/M_t \leq 1 \times 10^6$, and the target suffers no additional damage aside from the actual crater (Gault and Wedekind 1969; Fujiwara *et al.* 1977). It is also important to note that these craters fall into the energy range of the strength regime where $\sigma_t/\rho_t U^2 \sim 1$ (Gault and Wedekind 1969). Values for the present impacts are on the order of 10^5 and are listed in Table I. The features described above are consistent with descriptions of other impact craters produced in competent rock targets by Lange *et al.* (1984b), Gault (1973), Horz (1969), and Moore *et al.* (1963).

FRACTURES IN TARGETS

Bisecting the targets gave a detailed view of the internal fragmentation resulting from each impact. An example map of the distribution of these fractures in one of the gabbro targets is given in Fig. 5. The fractures visible without aid of magnification fall into seven classifications, which can be grouped into three different regions of the target. Most of the fractures occur in Region 1, a hemispherical area immediately below the crater extending outward for at least 10 projectile diameters. This region is characterized by a high density of small fractures, with the rock immediately below the crater floor being the most heavily crushed. These fractures are classified as "shear fractures" after the description in Moore *et al.* (1963). Also within this region are closely spaced "radial fractures" and larger "concentric fractures." Vertical cracks were found beneath the pit of several of the experimental craters. This phenomenon has been described by Fujiwara (1980) as a "central spallation fracture" resulting from the crossing of the two rarefaction waves formed by reflection at the vertical, free surfaces.

Outside Region 1 there are relatively few other visible fractures, and these fall into one of three very distinct categories. A se-

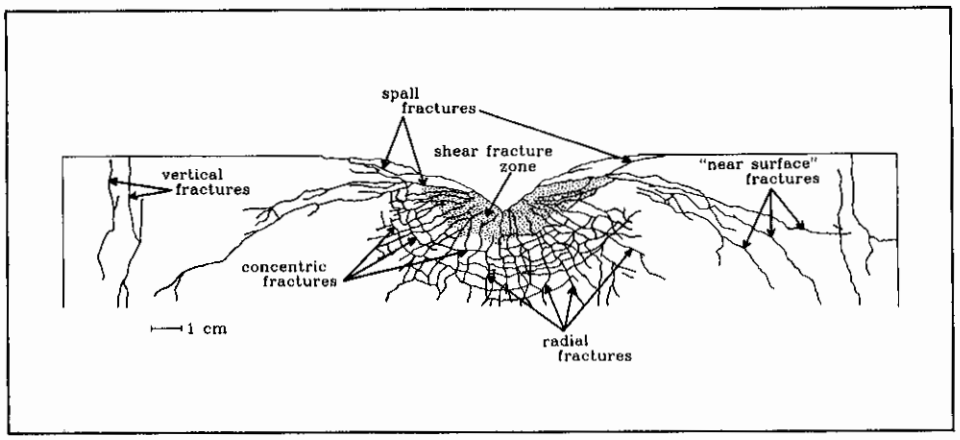

FIG. 5. Cross section of the target from shot 840904 illustrating the classification of internal fractures. Note that all fractures have been drawn with the same line thickness despite actual variations in the target. The shaded area immediately below the crater indicates a highly fractured region.

ries of vertical fractures are located close to and parallel to the vertical sides of the target blocks. These cracks are labeled as "side spallation fractures" after Fujiwara (1980), and are presumably due to reflections of the shock waves from the sides of the target. These fractures form the boundary for Region 2, which is the area where reflections from the target sides interfere with normal processes. This region will be virtually ignored in the remainder of the paper.

The third region is not really a region but a thin band of fractures starting at the crater wall and arcing down into the target. Subhorizontal fractures are found below and parallel to the floor of the proposed "spalled" zone. These fractures resemble the "spall fractures" observed by Maurer and Rinehart (1960) in several targets from very low-velocity, experimental impacts. The remaining fractures constitute a distinct category labeled "near-surface fractures" in Fig. 5. The origin of this terminology will become clear later in the Discussion section. The near-surface fractures are also radial in nature, although in general, they extend farther from the crater than those classified as "radial" above. In most cases, the fractures are bordered above and below by regions where the target is not visibly fractured. Finally, these fractures are much wider than most of the radial fractures immediately below the crater. In many cases, these fractures are the most prominent feature in the target cross section.

SPALL VELOCITY MEASUREMENTS

Analysis of the x-ray records from the two low velocity shots gives vertical spall velocity measurements of 11 m/sec and 17 m/sec for the lead and aluminum projectiles, respectively. These velocities are both less than 2% of the impact velocity. In these photographs large spall fragments are clearly distinguished from the smaller ejecta. The spall fragments appear to be ejected at an angle close to 90° from the target surface; however, at the time of the second x-ray exposure, the spalls had not yet completely separated from the target.

Vertical velocities were also measured from the framing camera films of the high-velocity Ames experiments. As evident in Fig. 2, the distinction between the spall fragments and the other ejecta is less obvious. This loss of resolution was partially the consequence of the scale of the photographs, and of a malfunction in the strobe

TABLE III

SPALL VELOCITY MEASUREMENTS

Shot No.	Spall No.	v_{min} (m/sec)	v_{ave} (m/sec)	v_{max} (m/sec)
603	1	8.7	11.0	13.5
608	1	17.0	17.3	17.6
840902	1	16.3	20.6	27.4
	2	10.2	14.8	17.2
840904	1	28.7	30.0	31.3
	2	17.5	23.1	26.4
	3	14.9	20.2	21.5
	4	9.0	11.7	17.6
	5	5.1	8.9	14.4
	6	0.7	2.6	3.6
840905	1a	22.4	23.6	24.1
	1b	20.8	22.8	25.3
	1c	19.3	21.5	23.7
	2	12.2	13.0	14.4
	3	9.4	10.8	12.3
	4	3.9	5.8	7.8
	5	0.7	1.2	2.6
	6	0.5	0.9	1.3
840907	1	15.6	17.6	18.8
	2	10.5	14.5	18.9
	3	9.8	13.0	16.5
	4	2.3	4.3	6.7

system that underexposed the films. However, since practically all of the larger fragments collected were spall fragments, it is likely that these velocity measurements correspond to spall fragments. Approximately 10 velocity measurements were taken for each particular fragment. In some cases there were large variations in velocity for a single fragment; therefore, the extremes in velocity as well as the average velocity are listed in Table III. The average vertical velocities ranged between 0.9 and 30 m/sec for the complete set of measurements. The results of the velocity measurements are plotted in Fig. 6. The error bars indicate not only the measurement errors but the range in velocities measured for each fragment. It is important to note that these velocities do not constitute a complete sampling of the spalls ejected from each event. Only the velocities of the largest fragments could be measured from the films. In addition, variations in velocity with time were observed for individual spall fragments. This may be partly a consequence of the usual spinning and tumbling of the fragments in flight.

It should be also noted that no attempt was made to measure the velocity of the prompt, high speed, nearly vertically traveling, ejecta. This material appears to be highly shocked by the direct impact of the projectile and is expected to represent the fine powder portion of the ejecta. We infer that this high-speed material is, for example, the 0.85 times impact velocity ejecta material reported by Curran *et al.* (1977).

Ejection angles could not be measured directly from only the two-dimensional films; however, ejection angles were determined for two of the spalls from shot 840905 by correlating the fragments on the films with those located after the event. The ejection angles measured for spalls 3 and 5 were 90 and 88°, respectively. Both frag-

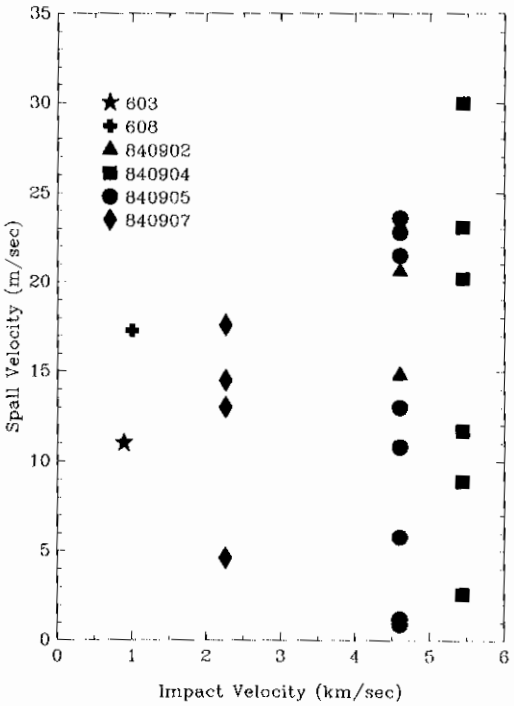

FIG. 6. Results of the spall velocity measurements for five experimental impacts.

ments were ejected at low velocities, so they did not interact with the tank walls.

Finally, in some cases the spalls were observed to fragment in flight as predicted by Melosh (1984). This appears to be the case for spalls 1a, 1b, and 1c from shot 840905. In addition to the appearance of fragmentation on the film, these three fragments are also traveling at approximately the same velocity with very little variation in individual velocities. However, it cannot be proven that this was actually fragmentation as opposed to merely an effect that was due to the resolution of the films.

DISCUSSION

Melosh (1984) derives two versions of a model based on the concept that the stress waves from an impact event are similar to those of an explosive source buried at some depth. First, a hydrodynamic ejection version of the model is presented using the interaction between a compressive wave and the corresponding tensile wave reflected from the target's free surface to predict spall velocities and thicknesses. Next, a stress wave ejection model is developed by adding the effect of a reflected shear wave to calculate ejection angles and fragment sizes. Fragment size is predicted to be inversely proportional to ejection velocity, and ejection angle is found to be a function of the target tensile strength and Poisson ratio. Although Melosh concludes that spallation is an unlikely mechanism for removing significant quantities of material from the Martian surface, it is potentially an important process for ejecting material from asteroids and possibly the Moon. The spallation model is also described and applied in Melosh (1987) and Vickery and Melosh (1987).

In order to explain the application of the spallation model to the present experiments, we first briefly review the relevant aspects of Melosh (1984) with emphasis on the hydrodynamic ejection version of the spallation model. One important feature of the spallation model is that there exists a region, the near-surface zone, where the target material experiences reduced compressive stress as a consequence of its proximity to a free surface. To satisfy the free surface boundary condition of zero stress, the compressive wave generated by a buried source is exactly canceled at the surface by the reflection of a tensile wave of equal magnitude. The actual definition of the depth of the source, the equivalent depth of burst, is up to dispute, but here we will use the form used in the spallation model, $d = 2a(\rho_p/\rho_t)^{1/2}$, for a projectile density ρ_p. It then follows that below the surface the two waves will superimposed by virtue of their finite rise and decay times. The near-surface zone is the region where the delay between the two waves is less than the rise time of the compressive wave. This region never experiences the peak of the compressive stress pulse, and is therefore the proposed source of the lightly shocked ejecta.

The depth of the near-surface zone is strongly controlled by the shape of the triangular stress pulse. The pulse shape will be characterized by a rise time, τ, and a decay time, τ_D, where τ is generally less than τ_D. For an impact, τ is modeled as being equal to a/U, where a is the projectile radius, and U is the impact velocity, and $\tau_D = d/c_L$. In this model the rise time is taken to remain constant as the shock propagates, although this may not be strictly true for small-scale impacts (Melosh 1984). The depth of the near-surface zone boundary is defined by the hyperbola in the s–z plane:

$$z_P = \frac{c_L\tau}{2}\left[\frac{4(d^2 + s^2) - c_L^2\tau^2}{4d^2 - c_L^2\tau^2}\right]^{1/2}, \quad (1)$$

where s is measured from the point of impact along the target surface. Figure 7 illustrates schematically the geometric relationships between s, d, and z_P. The values of τ and d calculated for each experiment are listed in Table IV. The last two entries in Table IV are two experiments taken from Lange *et al.* (1986b). The shot numbers

TABLE IV

RISE TIMES AND DEPTH OF BURST

Shot No.	τ (μsec)	d (cm)
603	4.4	1.55
608	3.9	0.75
840901	0.24	0.30
840902	0.34	0.52
840904	0.29	0.52
840905	0.34	0.52
840906	0.33	0.52
840907	1.0	0.47
840909	1.9	1.06
790837	0.30	0.54
790839	0.34	0.64

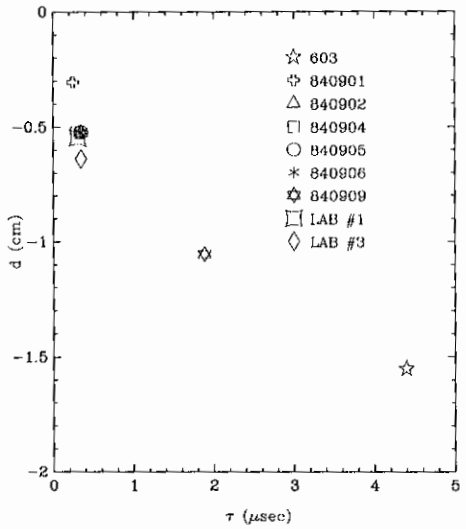

FIG. 8. Illustration of the range in values of the two major variables (depth of burst, d, and risetime, τ) for the present and some previous experiments.

790837 and 790839 correspond to shot No. 1 and 3, respectively, in Table II of Lange *et al.* (1986b). In order to illustrate the range of impact parameters between the eight experiments described above, the values for the depth of burst and the rise time are plotted in Fig. 8. These two parameters completely determine the shape of the near-surface boundary.

Physical evidence for the existence of the near-surface zone was suggested by the distribution of fractures observed in the bisected targets. As mentioned above, the category of "near-surface fractures" consisted of a set of major cracks forming a conspicuous pattern closely following the boundary of the near-surface zone as defined by Eq. (1). It is of considerable interest that no cracks were found above this region. A straightforward calculation of z_P for the relevant experimental parameters gives a remarkable fit of the near-surface zone boundary to the actual cracks observed in seven high-velocity experiments 840901, 840902, 840904, 840905, 840906, 790837, and 790839 (Figs. 9a–9c). Two of these targets, 790837 and 790839, are shots No. 1 and 3 taken from Lange *et al.* (1984b).

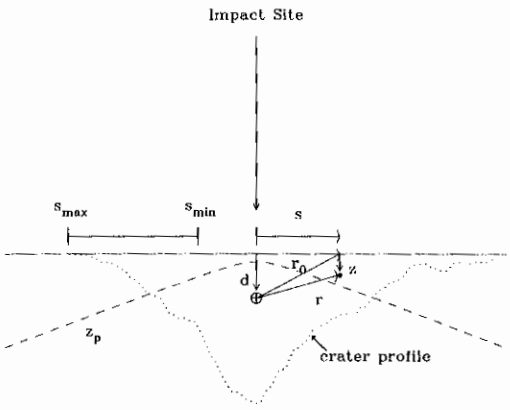

FIG. 7. Sketch of an experimental crater profile adapted from Melosh (1984). The relationships between the geometrical quantities s, z, r, r_0, and d are shown in relation to the crater depth profile from shot 840904. Also shown is an example of the range of s values, s_{min} to s_{max}, considered applicable for calculating spall velocities for this impact.

It should be noted that below the near-surface zone, radial cracks whose "center" is approximately a distance, d, below the impact point occurs. We infer that this radial cracking occurs during the compressive shock wave phase of cratering as a result of the tensile stresses concentrating about flaws (e.g., Sammis and Ashby 1986).

The first exception to this trend is in the target from 840909. Figure 9c shows that the near-surface fractures lie significantly above the calculated z_P curve for the relevant impact parameters. Although the total energy of this impact was comparable to that of the previous experiments, the impact velocity for this shot was substantially lower.

The second exception, 603, was also the result of a low-velocity impact. The target for shot 603 was qualitatively similar to those described above, although the radially fractured zone was significantly smaller. The most obvious feature in this target was one large crack beginning at the floor of the crater and extending in an arc to a depth of 6 cm. Although this crack had the same general form as the z_P boundary, it was asymmetric and did not match the curve defined by the parameters for that experiment. This is not unreasonable, since the projectile was a commercial bullet having a high density and a nonspherical shape. Determining the rise time of the stress wave from the geometry of the bullet is not straightforward. The radius of the bullet is not the same as the length over which the bullet starts as a point and reaches the maximum radius, which is also different from the bullet length. The curve for 603 in Fig. 9c was fit to this fracture by specifying the values of a and d to be 0.28 and 1.5 cm, respectively. This value for a, however, gives a rise time 28 percent less than that based on the bullet radius. Also, this depth of burst falls below the crater floor and is slightly greater than it would be if it were calculated with a 0.28-cm projectile radius. However, manipulating the equations to fit the fracture from this shot is not as important as recognizing its qualitative resem-

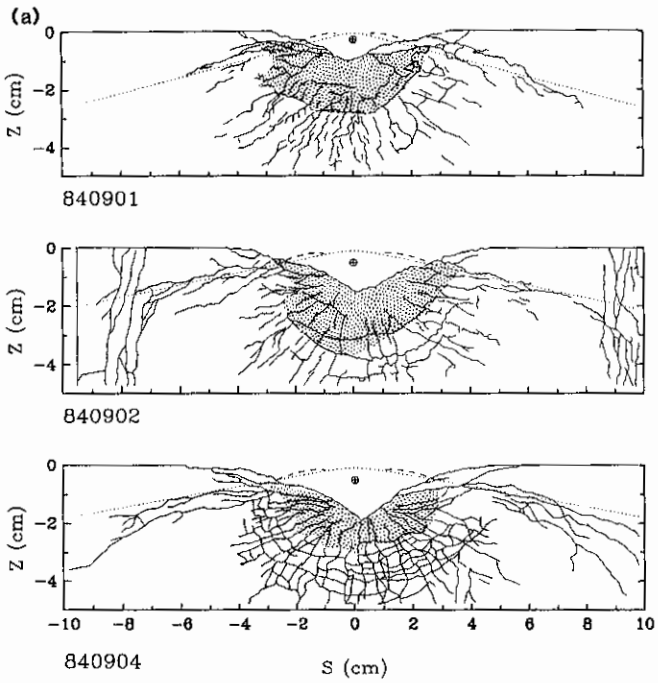

FIG. 9a. Sketches of the fractures found inside targets 840901, 840902, and 840904. The shaded area indicates the highly fractured region immediately surrounding each crater. A plot of z_P, the theoretical near-surface zone (dotted line), is superimposed over the fractures. The calculated spall thickness, z_S, is also plotted (dashed line) within the near-surface zone. The symbol below the surface of each target at $s = 0$ marks the equivalent depth of burst, d, used to calculate the curves.

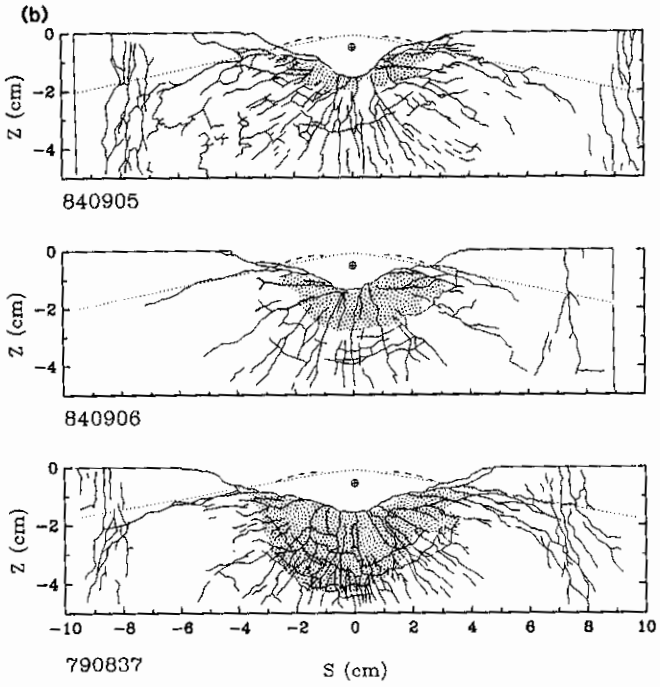

FIG. 9b. Sketches of the fractures found inside targets 840905, 840906, and 790837. The shaded area indicates the highly fractured region immediately surrounding each crater. A plot of z_P, the theoretical near-surface zone (dotted line), is superimposed over the fractures. The calculated spall thickness, z_S, is also plotted (dashed line) with the near-surface zone. The symbol below the surface of each target at $s = 0$ marks the equivalent depth of burst, d, used to calculate the curves.

blance to the fractures in the two other targets.

The same wave interaction should occur at the sides of the target as it does at the top surface, and a near-surface zone could be calculated as well. The vertical fractures near the target edges would be a candidate for this effect. However, the resulting boundary curve is much flatter and closer to the target surface. An example of this curve is plotted for shot 840906 in Fig. 9b; however, the boundary does not correlate with the vertical fractures observed.

Returning to the hydrodynamic ejection model, we consider its predictions for spall thicknesses as a function of s, and vertical spall velocity as a function of s and z. The spall thickness, defined as the depth at which the tensile stress reaches the dynamic tensile strength of the target material, is given as a function of s by

$$z_S = \left(\frac{\sigma_t}{P(r_0)}\right)\left(\frac{\tau_D c_L}{2d}\right)\left[\frac{r_0}{1 - 1.87\tau_D c_L/r_0}\right], \quad (2)$$

where $r_0 = \sqrt{s^2 + d^2}$, and is shown schematically in Fig. 7. The pressure at r_0 is determined by $P(r_0) = \rho_t c_L v_p(r_0)$, where $v_P(r) = (U/2)(\rho_p/\rho_t)(a/r)^{1.87}$ is the particle velocity at that point. This equation for z_S is valid only for z above the z_P boundary. The empirical quantity -1.87 comes from the exponent of pressure decay of the stress pulse in hard rock. Recent calculations by Ahrens and O'Keefe (1987) find this decay exponent to vary with impact velocity. Their results predict a pressure decay exponent of -1.87 for the impact of a silicate projectile on a silicate target at 9.8 km/sec. The relationship between z_P and z_S is also shown in the seven high-velocity experiments in Fig. 9. It is interesting to note that in agreement with the spallation model, z_S

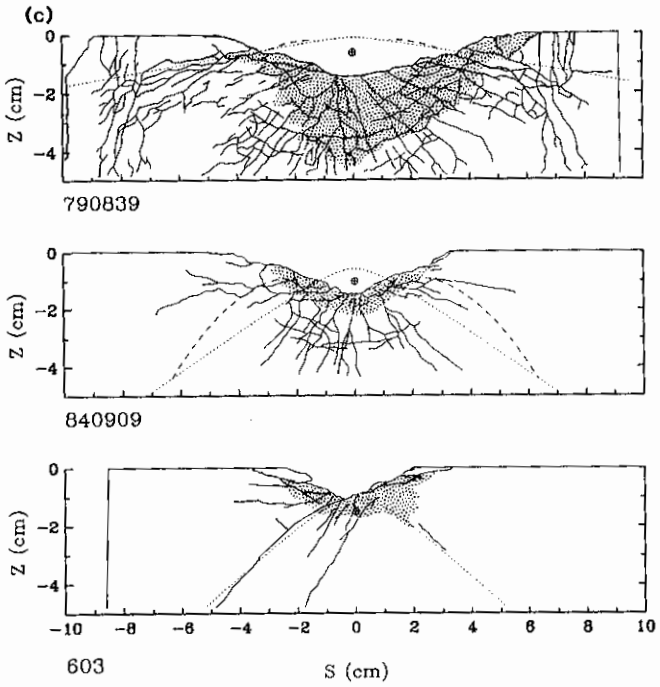

FIG. 9c. Sketches of the fractures found inside targets 790839, 840909, and 603. The shaded area indicates the highly fractured region immediately surrounding each crater. A plot of z_P, the theoretical near-surface zone (dotted line), is superimposed over the fractures. The calculated spall thickness, z_S, is also plotted (dashed line) within the near-surface zone. The symbol below the surface of each target at $s = 0$ marks the equivalent depth of burst, d, used to calculate the curves.

intersects the z_P curve at the edge of the observed crater.

Finally, the spall velocity is given for any $r = \sqrt{s^2 + (d - z)^2}$ within the near-surface region as

$$v_{V|SPALL} = 2v_P(r)\frac{d}{r_0}\left[1 - \frac{2dz_S}{r_0 c_L \tau}\right]. \quad (3)$$

The second term in the parentheses is negligible when the spall thickness is much smaller than all other dimensions. Then the spall velocity approaches the maximum value, $v_{V|SPALLmax} = 2v_P(r)d/r_0$. The spall thickness term can be neglected for large planetary scale impacts; however, it becomes significantly large in the calculations simulating the laboratory scale impacts. This term varies from 0.38 to beyond the limiting value of 1.0 in the present experiments. Therefore, the predicted velocities for the laboratory impacts can be at most 62% of the maximum spall velocity. It must also be noted that Eqs. (2) and (3) are not valid for s less than approximately four projectile radii from the point of impact. For small s, z_S becomes negative as a result of certain approximations made earlier in the model. This point will be discussed later.

Although $v_{V|SPALL}$ is a function of both s and z, the calculated spall velocities in Fig. 10 are the results of the spallation model applied to the laboratory parameters for the limiting case of $z = 0$. This limiting case represents the maximum velocity possible at any given s. The appropriate experimental values of U, a and ρ_p were used with Eq. (3) to generate each curve in Fig. 10. (The steep, unphysical, decrease in velocity toward the center of the crater is a result of z_S becoming negative at small s, is not shown. This portion of the curve can be neglected.) Shaded rectangles are included on each plot to compare the spallation model results with the experimental results. The vertical

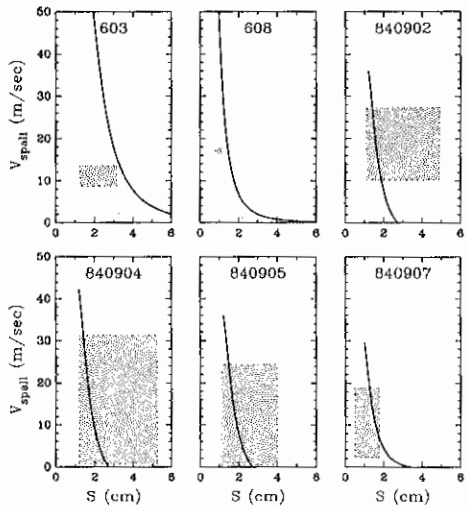

FIG. 10. Vertical spall velocity, as calculated from the Melosh equations evaluated at $z = 0$, is plotted as a function of s to model five of the experimental impacts. The rectangles provide a comparison of the experimental results to the dotted model curves. The range of measured spall velocities for each event is indicated by the height of the rectangles. The horizontal extent of the rectangles represents the range of s, s_{min} to s_{max}, measured from the spalled zone of each crater (as illustrated in Fig. 3).

sides of each rectangle represent the range of spall velocities measured experimentally. The horizontal sides of the rectangles limit the range of s to the spalled region measured from each of the craters (Fig. 7). In all the high-velocity experiments, the model velocity curves intersect the measured velocity fields and reach from 64 to 76% of the peak in the velocity profile predicted by the spallation model. The spall velocities measured for the low-velocity experiments account for a lower percentage of the predicted velocities; however, it is important to note that these two experiments have only one velocity measurement per impact. Although the spall velocities measured in these experiments are only a fraction of the velocities predicted by the model (Fig. 10), it is important to realize that the model curves represent the maximum surface velocity at any distance from the impact. Furthermore, the spallation model predicts a strong decrease of spall velocity with depth. Since each spall fragment has a finite thickness, its average velocity would be lower than that predicted for a point on the surface. Therefore, the present results compare well with the spallation model, despite the fact that these equations were formulated for conditions much different from those found in small-scale laboratory impacts.

The effect of this scale difference becomes more severe for low-velocity impacts. Equations (2) and (3) are difficult to apply to shots 603 and 608, because the projectile radius is quite large compared to the resulting crater. Thus, the depth of burst calculated according to the above formula is also greater than the actual crater depth. Nevertheless, for these shots, rough estimates of spall velocity were calculated for Fig. 10 by adjusting d to equal the depth of the crater. In the case of shot 603, this d turns out to be above the depth of burst determined earlier when fitting the z_P curve to the large fracture.

Although the assumption that spall thicknesses are much smaller than the projectile radius has been violated in most cases, the Ames experiments are more similar to the conditions described by the spallation model. The higher impact velocities in these experiments lead to the strong stress waves needed to satisfy the hydrodynamic approximations. In addition, the Ames projectile radii were smaller than those of the preliminary experiments. This feature, combined with the higher impact velocities, produced shorter rise times for these impacts, which is desirable because the approximations also require that r be greater than $c_L\tau$. Therefore, Equations (2) and (3) could be applied throughout a greater fraction of the crater volume in the high-velocity experiments.

SUMMARY AND CONCLUSIONS

Analysis of the interior of six out of eight targets revealed the absence of visible fractures above the predicted boundary of the near surface zone. Furthermore, in the six high-velocity experiments the theoretical z_P

boundary could be linked to definite fractures observed in the targets. This correlation gives physical support to the spallation model, and indicates that the material above this boundary may be less highly shocked than target material at a similar radial distance below the boundary. However, a physical mechanism for the formation of these fractures is not obvious.

The measured spall velocities are consistent with the vertical spall velocities predicted by the hydrodynamic spallation model. This statement is valid despite the assumptions inherent in this model, which restrict its application to laboratory impacts. The spall velocities measured were all less than a few percent of the respective impact velocities. The greatest average spall velocity measured, 30 m/sec, was for shot 840904 and was only 0.6% of the 5.4 km/sec impact velocity.

Scaling this measured spall velocity to that expected for a large impact is difficult if we are restricted only to the equations presented in the above discussion. One simple alternative is to examine the basic functional dependencies of Eq. (3). We see that spall velocities are primarily a function of impact velocity and the distance from the impact point normalized to the projectile radius, suggesting that spall velocities resulting from the impact of an asteroid traveling at 5 km/sec on a silicate planet would directly scale with s/a to those velocities measured experimentally. If we now consider impacts upon small bodies in the solar system we must first neglect the effects of a regolith. In such a case, the 27 m/sec spall velocity we measure would enable fragments to escape only parent satellites or asteroids less than 46 km in diameter. While this criteria would include the Martian satellites Phobos and Diemos, it would exclude the larger, presumably igneous and differentiated, asteroids such as Ceres and Vesta.

However we note that a more detailed stress-wave ejection version of the spallation model for impacts of larger bodies may permit the possibility of high-speed spallation fragments. Although these were not observed in the present experiments or calculations, a more detailed model would not suffer from the restriction that the fragments must originate from regions farther than four projectile radii from the point of impact. Melosh (1987) has constructed such a model and provides a plot of spall velocities as a function of depth for s between one and five projectile radii. His more recent results predict spall velocities in excess of 13% of the impact velocity for s/a less than 1.4. For the present experimental impacts, the projectile radii are as small as 0.159 cm. Therefore, if these high-velocity spalls exist, they could not be observed on the films. Even for large impacts, the high-velocity fragments would be a small fraction of the spall fragments ejected. Using this argument, Melosh predicts spalls capable of escaping the Moon but not Mars. However, the present results support the spallation model velocity only at its lower limits where the spall fragments are large enough to be observed.

ACKNOWLEDGMENTS

We have benefited from technical discussions with Jay Melosh and technical reviews from A. Vickery and A. Fujiwara. We thank Peter Schultz for his assistance in utilizing the Ames facility. This research was supported by NASA Grant NGL-05-002-105. Contribution 4405, Division of Geological and Planetary Sciences, California Institute of Technology, Pasadena, California.

REFERENCES

AHRENS, T. J., AND J. D. O'KEEFE 1987. Impact on the Earth, ocean, and atmosphere. Proc. 1986 Hypervelocity Impact Symp., *Int. J. Impact Eng.* **5**, 13–32.

AHRENS, T. J., AND J. D. O'KEEFE 1978. Energy and mass distributions of impact ejecta blankets on the Moon and Mercury. *Proc. Lunar Planet. Sci. Conf. 9th*, 3787–3802.

BIRCH, F. 1966. Compressibility: Elastic constants. In *Handbook of Physical Constants* (S. Clark, Jr., Ed.), *Geol. Soc. Amer. Mem.* **97**, 97–173.

CAPACCIONI, F., P. CERRONI, M. CORADINI, M. DI MARTINO, P. FARINELLA, E. FLAMINI, G. MARTELLI, P. PAOLICCHI, P. N. SMITH, A. WOODWARD, AND V. ZAPPALA 1986. Asteroidal catastrophic col-

lisions simulated by hypervelocity impact experiments. *Icarus* **66,** 487–514.

CINTALA, M. J., J. W. HEAD, AND L. WILSON 1979. The nature and effects of impact cratering on small bodies. In *Asteroids* (T. Gehrels, Ed.), pp. 579–600. Univ. of Arizona Press, Tuscon.

CURRAN, D. R., D. A. SHOCKEY, L. SEAMAN, AND M. AUSTIN 1977. Mechanisms and models of cratering in earth media. In *Impact and Explosion Cratering* (D. J. Roddy, R. O. Pepin, and R. B. Merrill, Eds.), pp. 1057–1087. Pergamon Press, New York.

FUJIWARA, A. 1980. On the mechanism of catastrophic destruction of minor planets by high-velocity impact. *Icarus* **41,** 356–364.

FUJIWARA, A., G. KAMIMOTO, AND A. TSUKAMOTO 1977. Destruction of basaltic bodies by high-velocity impact. *Icarus* **31,** 277–288.

GAFFNEY, E. S. 1978. Effects of gravity on explosion craters. *Proc. Lunar Planet. Sci. Conf. 9th,* 3831–3842.

GAULT, D. E. 1973. Displaced mass, depth, diameter, and effects of oblique trajectories for impact craters formed in dense crystalline rocks. *Moon* **6,** 32–44.

GAULT, D. E., AND J. A. WEDEKIND 1969. The destruction of tektites by micrometeroid impact. *J. Geophys. Res.* **74,** 6780–6794.

HORZ, F. 1969. Structural and mineralogical evaluation of an experimentally produced crater in granite. *Contrib. Min. Petrol.* **21,** 265–277.

LANGE, M. A., T. J. AHRENS, AND M. B. BOSLOUGH 1984a. Cratering and spall fracture in gabbro. Chapter XI:7, In *Shock Waves in Condensed Matter 1983* (J. R. Asay, R. A. Graham, and G. K. Straub, Eds.), pp. 525–528. Elsevier Science Publishers B.V.

LANGE, M. A., T. J. AHRENS, AND M. B. BOSLOUGH 1984b. Impact cratering and spall failure of gabbro. *Icarus* **58,** 383–395.

MARVIN, U. B. 1984. A meteorite from the moon. *Smithson. Contrib. Earth Sci.* **26,** 95–103.

MAURER, W. C., AND J. S. RINEHART 1960. Impact crater formation in rock. *J. Appl. Phys.* **31,** 1247–1252.

MCSWEEN, H. Y. 1985. SNC Meteorites: Clues to Martian petrologic environment? *Rev. Geophys.* **23,** 391–416.

MCSWEEN, H. Y., AND E. STOLPER 1980. Basaltic meteorites. *Sci. Amer.* **242,** 54–63.

MELOSH, H. J. 1987. High-velocity solid ejecta fragments from hypervelocity impacts. Proc. 1986 Hypervelocity Impact Symp., *Int. J. Impact Eng.* **5,** 483–492.

MELOSH, H. J. 1985. Ejection of rock fragments from planetary bodies. *Geology* **13,** 144–148.

MELOSH, H. J. 1984. Impact ejection, spallation, and the origin of meteorites. *Icarus* **59,** 234–260.

MOORE, H. J., D. E. GAULT, AND R. V. LUGN 1963. Experimental impact craters in basalt. *Trans. Soc. Mining Eng.* **226,** 258–262.

O'KEEFE, J. D., AND T. J. AHRENS 1985. Impact and explosion crater ejecta, fragment size, and velocity. *Icarus* **62,** 328–338.

POLANSKEY, C. A., AND T. J. AHRENS 1985. Spall velocity measurements of laboratory scale impact craters (abstract). In *Lunar Planet. Sci. XVI,* pp. 671–672. Lunar and Planetary Institute, Houston.

SAMMIS, C. G., AND M. F. ASHBY 1986. The failure of brittle porous solids under compressive stress states. *Acta Metall.* **34,** 511–526.

STUMP, B. W., AND R. E. REINKE 1984. Spall observations and mechanisms in alluvium. *J. Geophys. Res.* **89,** 495–506.

VICKERY, A. M. 1986. Size-velocity distribution of large ejecta fragments. *Icarus* **67,** 224–236.

VICKERY, A. M., AND H. J. MELOSH 1987. The large crater origin of SNC meteorites. *Science* **237,** 738–743.

WOOD, C. A., AND L. D. ASHWAL 1981. SNC meteorites: Igneous rocks from Mars. *Proc. Lunar Planet. Sci. Conf.* **12B,** 1359–1375.